Journal of Materials Chemistry C

Examining the electron transport in chalcogenide perovskite BaZrS3

Journal:	*Journal of Materials Chemistry C*
Manuscript ID	TC-ART-01-2021-000374.R1
Article Type:	Paper
Date Submitted by the Author:	15-Feb-2021
Complete List of Authors:	Osei-Agyemang, Eric; Lehigh University, Mechanical Engineering Koratkar, Nikhil; Rensselaer Polytechnic Institute, Mechanical Engineering Balasubramanian, Ganesh; Lehigh University, Mechanical Engineering; Lehigh University,

Examining the electron transport in chalcogenide perovskite $BaZrS_3$

Eric Osei-Agyemang[1], Nikhil Koratkar,[2] and Ganesh Balasubramanian[1,a]

[1] *Department of Mechanical Engineering and Mechanics, Lehigh University, 19 Memorial Drive West, Bethlehem, PA 18015, USA*

[2] *Department of Mechanical, Aerospace and Nuclear Engineering and Department of Materials Science and Engineering, Rensselaer Polytechnic Institute, Troy, NY 12180, USA*

ABSTRACT

Orthorhombic $BaZrS_3$ is a potential optoelectronic material with prospective applications in photovoltaic and thermoelectric devices. While efforts exist on understanding the effects of elemental substitution and material stability, fundamental knowledge on the electronic transport properties are sparse. We employ first principles calculations to examine the electronic band structure and optical band gap and interrogate the effect of electron transport on electrical and thermal conductivities, and Seebeck coefficient, as a function of temperature and chemical potential. Our results reveal that $BaZrS_3$ has a band gap of 1.79 eV in proximity of the optimal 1.35 eV recommended for single junction photovoltaics. An absorption coefficient of 3×10^5 cm^{-1} at photon energies of 3 eV is coupled with an early onset to optical absorption at 0.5 eV, significantly below the optical band gap. The carrier effective mass being lower for electrons than holes, we find the Seebeck coefficient to be higher for holes than electrons. A notable ($\approx$ 1.0 at 300 K) upper limit to the thermoelectric figure of merit, obtained due to high Seebeck coefficient (3000 μV/K) and ultra-low electron thermal conductivity, builds promise for $BaZrS_3$ as a thermoelectric.

[a] Corresponding author. Email: bganesh@lehigh.edu. Phone: +1 610 758 3784;
Address: Packard Laboratory 561, 19 Memorial Drive West, Bethlehem, PA 18015, USA.

INTRODUCTION

Chalcogenide perovskites have gained increased attention from the scientific community due to their promising photovoltaic and thermoelectric properties. These perovskites form in the ABX_3 configuration with A and B being elements with combined valence of 6 (generally containing Group-IIA elements such as Ba, Ca and Sr and Group-IVB elements such as Hf, Zr, and Ti) and X typically being S or Se. As these constituent elements are considered less toxic and gentle on the environment relative to, for instance, Pb in organic-inorganic halide perovskites, some of these compounds have been synthesized experimentally,[1–6] mostly in the needle-like phase (NH_4CdCl_3),[1,7] the hexagonal phase ($BaNiO_3$),[2,8] or as the orthorhombic distorted perovskite ($GdFeO_3$).[4] Among the recently examined chalcogenide perovskites, $BaZrS_3$ has demonstrated strong potential for photovoltaics since the calculated band gap of 1.76 – 1.82 eV[9,10] is in the neighborhood of ~1.35 eV that is also considered optimum for energy-conversion applications.[11] While reports exist on $BaZrS_3$ for alloying and defect control,[12] stability and band gap tuning,[13] the effect of substituting S for O in $BaZrO_3$ and the subsequent band gap[14] and phonon transport properties,[15] efforts towards understanding the fundamental electron mediated transport mechanisms, and quantifying the electronic properties, are absent. Such knowledge is key to evaluate the applicability of $BaZrS_3$ for thermoelectric and optoelectronic devices. Here, we employ density functional theory (DFT) calculations together with Boltzmann transport equation to examine the electrical and electron thermal conductivities, in addition to the optical absorption spectrum of $BaZrS_3$ in its orthorhombic distorted perovskite structure. Our predictions, as elaborated below, reveal that strong anisotropic effects impact the conductivities along specific lattice directions under doping, and the material possesses high absorption coefficients ($>10^5$ cm^{-1}) with an early onset of photon absorption significantly prior to the fundamental band gap.

RESULTS AND DISCUSSION

The lattice constants of the $BaZrS_3$ structure are well reproduced from our first principles calculations, and in excellent agreement with experimental measurements.[4] The calculated lattice parameters of the distorted perovskite structure are listed in Table 1. Note that, in addition, a precise representation of the electronic band structure is required from the computations to accurately estimate the electronic properties. Our calculations predict a direct band gap of 1.79 eV

at the Γ point (0.0, 0.0, 0.0). This result is in excellent agreement with experimentally measured values of 1.73-1.85 eV.[2,12,13,16] Additionally, our calculated band gap using the hybrid HSE06 functional concurs with other theoretical calculations that employ the same functional with estimates of 1.75 eV,[9] 1.76 eV,[12] 1.7 eV,[16] 1.7 eV,[14] and 1.82 eV.[10] Calculations using other functionals tend to underestimate the band gap of $BaZrS_3$ with the PBE functional rendering a value of 1.02 eV, while the GGA+U functional with a U parameter of 4.5 eV yields a band gap of 1.72 eV.[12] These observations attest to the validity of the hybrid HSE06 functional used to predict the electronic band gap necessary for an accurate description of the charge transport mechanisms.

The electronic band structure and the density of states (DOS) are illustrated in Figure 1. The band structure shows that the valence band maximum (VBM) and the conduction band minimum (CBM) are composed of S- *3p* states and Zr- *4d* states, respectively, at the Γ point.

Table 1: The calculated lattice parameters and band gap for orthorhombic distorted $BaZrS_3$ perovskite are listed, and are in excellent agreement with experimental measurements.

	Lattice parameter (Å)			Band gap (eV)
	a	b	c	
This work	7.066	9.923	6.972	1.79
Experiment	7.060[4]	9.980[4]	7.030[4]	1.73-1.85[2,12,16]

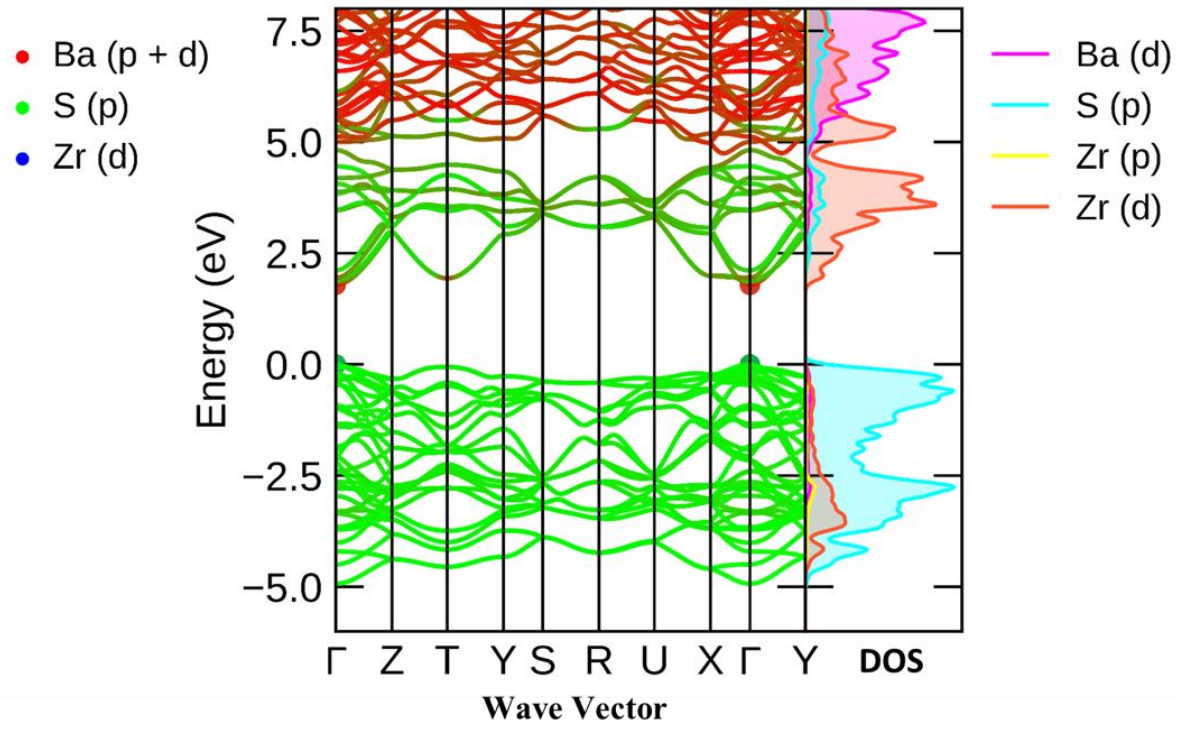

Figure 1: Electronic band structure and projected density of states (DOS) for $BaZrS_3$ orthorhombic distorted perovskite. The calculated direct band gap at the Γ (0.0, 0.0, 0.0) point is 1.79 eV.

A deeper scrutiny of the VBM and CBM suggests the bands as dispersive, as also noted from the DOS. This behavior is attributed to the more disperse and less localized Zr -*4d* states and the S-*3p* states. The conduction band reveals antibonding energy states between Zr- *4d* and S- *3p* orbitals, while the valence band suggests bonding states between Zr -*4d* and S -*3p* states. The dispersive nature of the band edges implies low carrier effective masses that contribute to efficient carrier transport. We calculate the electron (hole) effective masses along the Γ-X, Γ-Y and Γ-Z directions as 0.347 (-0.556), 0.218 (-0.253) and 0.422 (-0.747) fractions of m_o (electron rest mass), respectively. Irrespective of whether electrons or holes act as the predominant carriers, enhanced transport properties are expected along the *a* and *b* lattice directions. We also expect notable carrier transport properties for $BaZrS_3$ given the calculated carrier effective mass is less than 1.0 m_o. The optical absorption spectra presented in Figure 2 provides insights into the ultraviolet-visible (UV-Vis) optical absorption of $BaZrS_3$ as well as the imaginary part of the dielectric constant, ε_2, that determines the absorption properties of the chalcogenide perovskite.

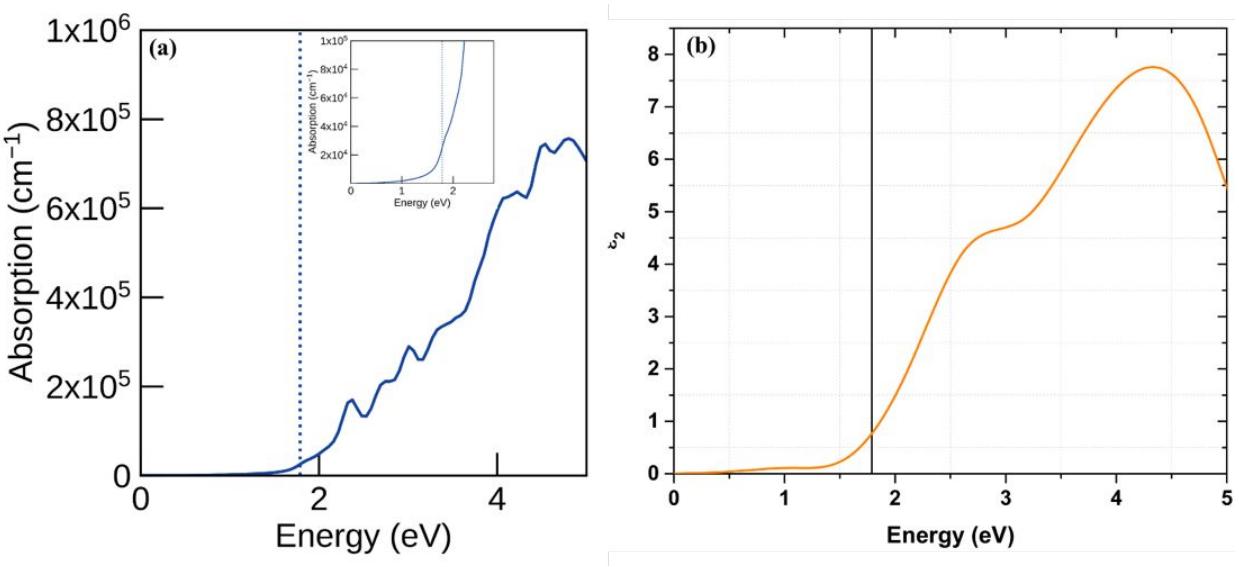

Figure 2: (a) UV-VIS absorption spectrum and **(b)** imaginary part of the dielectric constant (ε_2) for $BaZrS_3$ in the orthorhombic distorted perovskite phase. The inset in figure (a) displays magnified area of photon energies before the optical band gap of 1.79 eV. The vertical lines signify the position of the optical band gap of $BaZrS_3$.

The optical absorption of $BaZrS_3$ initiates around photon energies of ~ 0.5 eV, indicating that the perovskite has an early onset for optical absorption even before the fundamental band gap is attained. This early onset of optical absorption is dependent on the material, temperature and the range of wavelengths considered. This phenomenon is typically due to free-carrier absorption by either free electrons or free holes, inter-valence-band absorption by holes or inter-conduction-band absorption by electrons. One or more of these mechanisms dominate depending on the relative concentration of electrons or holes in the material. For intrinsic materials, both the electron and hole contributions play an important role.[17]

The distorted $BaZrS_3$ structure achieves its highest UV-Vis absorption at ~ 4.8 eV of photon energy. As photons with energy less than 3.4 eV contribute to the majority of solar energy reaching the earth's surface,[9] $BaZrS_3$ holds promise as a photovoltaic material, and attains a highest optical absorption of ~ 3×10^5 cm^{-1} at ~ 3 eV. The optical absorption properties are typically attributed to

the *d* orbitals located at the band edges.[9] This large absorption coefficient suggests the photovoltaic efficiency of $BaZrS_3$ is not solely influenced by carrier mobility. Also, for the maximum solar spectral irradiance that occurs at an incident photon energy of ~ 2.5 eV,[9] $BaZrS_3$ is estimated to possess optical absorption of 2×10^5 cm^{-1}, which makes it a potential material for solar thin film applications. $BaZrS_3$ obtains its highest $\varepsilon_2 = 7.9$ at photon energy of ~ 4.3 eV, although $\varepsilon_2 = 4.5$ acquired at 2.7 eV is higher than that estimated for advanced solar materials, such as CdTe and GaAs, at the same photon energy.[9]

Solution to the Boltzmann transport equations through the BOLTZTRAP code[18] is used to predict the Seebeck coefficient (S), the electrical conductivity (σ) and the electron thermal conductivity (κ_e) along the *a*, *b*, and *c* lattice directions of the distorted perovskite for different chemical potentials (μ) and temperatures (T). We employ the constant relaxation-time (τ) approximation since it is difficult to estimate τ given the occurrences of different scattering mechanisms (at the boundaries, between carriers, etc.) in the material. We calculate $\tau = 10^{-14}$ s, similar to previous reports[19,20]. Moreover, $\tau = 10^{-14}$ s was recently calculated for the chalcogenide perovskite $CaZrSe_3$[21]. The upper limit of the thermoelectric figure of merit (ZT_e), however, does not depend on τ.

The variation of the power factor ($PF = S^2\sigma$) and ZT_e over a range of carrier concentrations from $10^{15} – 10^{22}$ cm^{-3} across different temperatures are presented in Figures S1 and S2 (supplementary information), respectively. At lower temperatures (< 600 K), higher *PF* values are noted for *p*-type doping, while *n*-type doping yields higher values at temperatures > 600 K. The highest *PF* values are achieved at 10^{21} cm^{-3} for both *p*- and *n*-type doping at all temperatures, with *PF* increasing with temperature. Increased *PF* values are obtained for higher carrier concentrations relative to lower ones. From the Bethe-Sommerfeld expansion of the Mott relation for degenerate statistics and single band conduction, we have $S = \frac{\pi^2 k_B^2 T}{3\ e}\left[\frac{DOS(E)}{n(E)} + \frac{1}{\varphi(E)}\frac{d\mu(E)}{dE}\right]_{E=E_F}$, where e is the carrier charge, $DOS(E)$ is the energy-dependent electronic density of states, $n(E)$ is the energy dependent number of states, k_B is the Boltzmann constant, and φ is the energy dependent carrier mobility. S is inversely proportional to φ and hence a high effective mass (*i.e.*, low carrier mobility) yields higher *PF*s.[22] The average effective mass for holes is higher than that for electrons, resulting in an enhanced *PF* when placing higher emphasis on the contribution of S to *PF*. As the doping concentration increases, σ increases and S decreases; thus, there exists an optimum *PF* at relatively

high carrier concentrations in the proximity of the conduction band (here, that carrier concentration being 10^{21} cm^{-3}).[23] From Figure S2, we find that higher ZT_e is achieved for lower (10^{15} – 10^{18} cm^{-3}) rather than higher carrier concentrations. ZT_e is rooted to the entropy production in a thermoelectric energy conversion process, and higher carrier concentration contributes to an increased entropy production that drastically reduces the ZT_e. On the other hand, at higher temperatures, κ_e increases due to the relatively higher number of excited electrons, thereby decreasing ZT_e. The calculated ZT_e values are similar for *p*- and *n*-type doping (~ 1.0) between 100 – 700 K. The highest $ZT_e \approx 1.0$ occurs at 300-700 K at carrier concentrations of 10^{15}-10^{18} cm^{-3}. ZT_e decreases with increasing carrier concentration across all temperatures. From Figure S3 (supplementary information), the variation of carrier concentration from 1×10^{17} to 9×10^{17} cm^{-3} suggests that the highest ZT_e for 100 – 700 K is achieved at 10^{17} cm^{-3}. Combining the distributions for *PF* and ZT_e against chemical potential and temperature, we hence predict the electronic transport properties at a carrier concentration of 10^{17} cm^{-3}, as also suggested in the literature for optimal photovoltaic performance of $BaZrS_3$.[12]

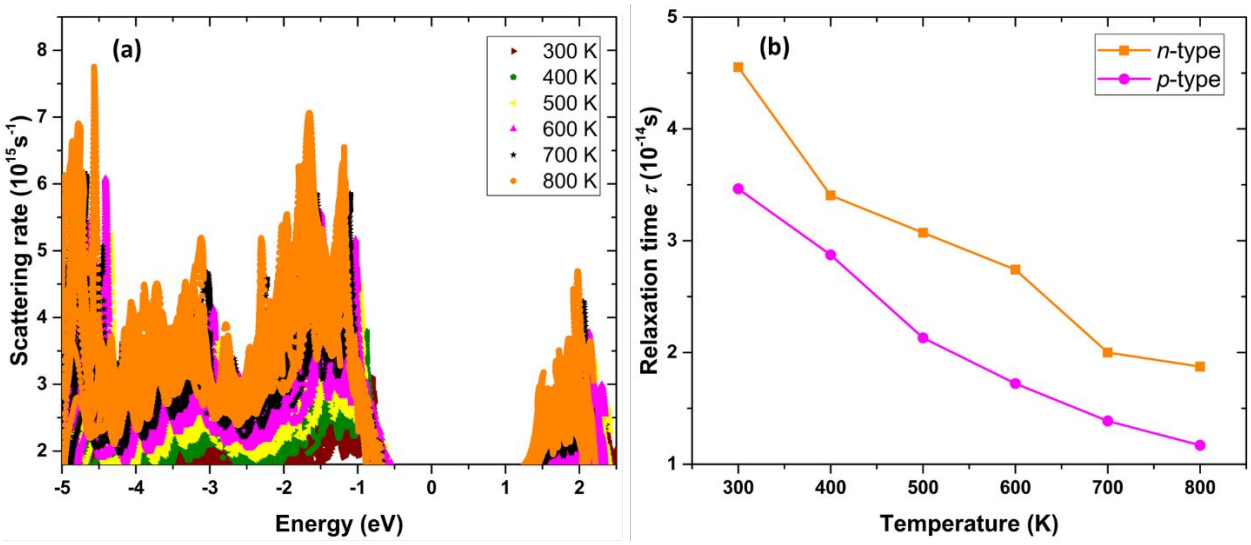

Figure 3: (a) The scattering rate as a function of energy and **(b)** the carrier relaxation time τ as a function of temperature for electrons (*n*-type) and holes (*p*-type). The extracted carrier relaxation time is 10^{-14} s.

The electron-phonon scattering rate as a function of energy across a temperature range from 300-800 K is obtained as the reciprocal of the relaxation time ($1/\tau_{nk}$), and presented in Figure 3(a).

The illustration depicts the shape of the DOS that demonstrates the available phase space for carrier scattering. This phase space provides the available volume and area within which three-phonon scattering processes such as absorption and annihilation occur as well as the electron-phonon coupling which results in scattering of the charge carriers. The density of states at the different energy levels shown in Figure 3(a) provides an estimate of the available phase space at such energies where the electron-phonon coupling processes occurs. For instance, at 800 K, within an energy window of -1 eV to -5 eV, the available phase space is larger than the energy window of -2 eV to -3 eV. The resulting lower carrier relaxation times at higher temperatures is evidenced by the increase in scattering rate with temperature. In Figure 3(b), the relaxation time for holes(electrons) are extracted from the valence band maximum (conduction band minimum) which suggests that electrons assume higher relaxation times relative to holes. Increased scattering at higher temperatures leads to decrease in the relaxation times. Figure 3(b) yields a relaxation time in the order of 10^{-14} s at different temperatures for $BaZrS_3$.

The temperature and directional dependence for S, σ, κ_e and PF in $BaZrS_3$ for p-type doping are presented in Figure 4 (the corresponding variations for n-type doping are in Figure S4 as supplementary information). S increases steeply from 50 K to 300 K, gradually from 300 K to 850 K and decreases at $T > 850$ K. This phenomenon is explained by the fact that S is a metric for the average entropy transported by a charge carrier per unit charge in the limit of thermal equilibrium; hence S decreases (or increases) with reducing (or rising) temperatures.[24]

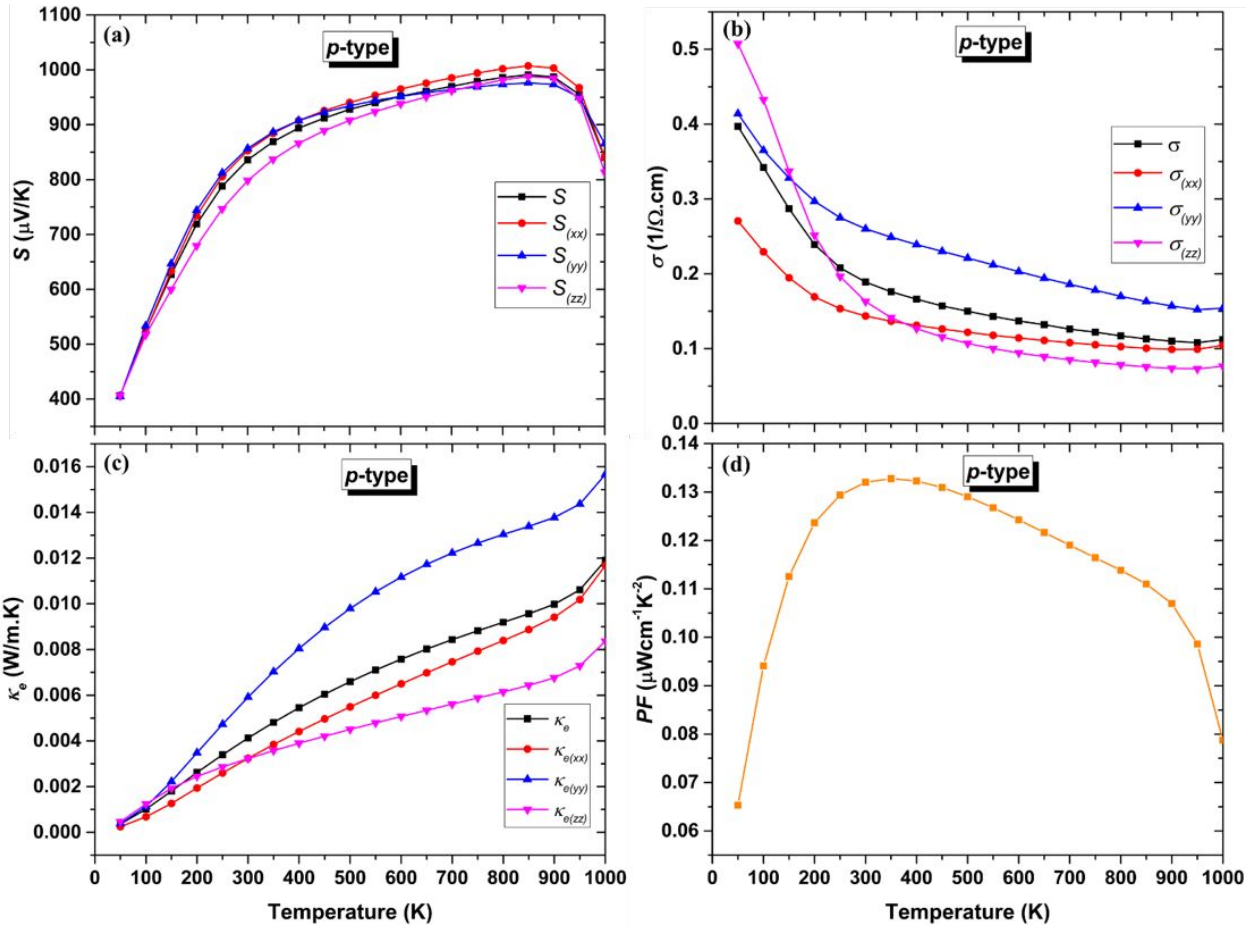

Figure 4: Electronic transport properties of $BaZrS_3$ at a carrier concentration of 10^{17} cm^3 for p-type doping. **(a)** Seebeck coefficient S with anisotropic contributions from all three crystallographic directions, **(b)** electrical conductivity σ along the *a, b* and *c* crystal lattice directions, **(c)** electronic thermal conductivity κ_e along the lattice directions, and **(d)** power factor *PF* at different temperatures. There are significant anisotropic effects in the thermoelectric properties at all temperatures, especially for σ and κ_e. The highest *PF* is achieved at 350 K.

At 300 K, $S \approx 820$ μV/K for *p*-type doping, while $S \approx 620$ μV/K for *n*-type doping. The calculated S is higher for $BaZrS_3$ (*p*-type) relative to $CaZrS_3$, but comparably lower for *n*-type doping,[21] because S is inversely proportional to the carrier mobility and higher carrier mobility are calculated for *p*-type doping in $CaZrSe_3$ compared to $BaZrS_3$ while the opposite is observed for *n*-type doping. Minor anisotropic effects are observed in S between 200 – 850 K, while no such effects are noted in case of *n*-type doping. This directional dependence can be utilized when designing a $BaZrS_3$

based thermoelectric device to yield optimum performance along specific crystallographic directions.

σ decreases steeply at $T < 300$ K while a more gradual reduction is noted thereafter (Figure 4(b)), in contrast to the trend observed for S. The decrease in σ with increasing temperature occurs due to presence of more excited electrons and enhanced electron scattering. At 300 K, the average $\sigma \approx 0.20\ \Omega^{-1}cm^{-1}$ is lower than the mean value ($0.68\ \Omega^{-1}cm^{-1}$) predicted for $CaZrSe_3$,[21] and significantly lower than that of competing electronic materials, such as SnSe, GeS, GeSe and SnS.[20] However, σ assumes a higher magnitude of $0.62\ \Omega^{-1}cm^{-1}$ under n-type doping because of the low carrier effective mass for electrons relative to that for the holes. σ also depends on the choice of the carrier relaxation time τ since a lower τ will result in a higher σ. The highest σ is recorded along the a and b lattice directions for both p-type and n-type doping and for $T > 150$ K. This finding is attributed to the lower carrier effective mass (high carrier mobility) along the a and b lattice directions (-0.556 m_o and -0.253 m_o, respectively) for p-type doping, and likewise (0.347 m_o and 0.218 m_o, respectively) for n-type doping. However, we note that there is a slight deviation in σ at $T < 150$ K for p-type doping, possibly due to computational uncertainties. A similar observation is made for the phonon transport properties of $BaZrS_3$ along the different lattice directions. Though the magnitude of the anisotropy in the lattice thermal conductivity is minute, enhanced phonon transport properties are observed along the b- and a- lattice directions while lower lattice thermal conductivity is predicted along the c- direction.[15] Additionally, the $BaZrS_3$ lattice parameters along the a- and b- directions are higher than the c- direction, which leads to longer phonon mean free path along these directions before annihilation. As similar observations are made for the electron(hole) and phonon transport properties along the different lattice directions, we expect strong electron-phonon coupling along the a- and b- lattice directions and subsequently higher carrier scattering along these directions. When designing efficient photovoltaic and thermoelectric $BaZrS_3$ based devices, the different transport properties along the various lattice directions could be modified to achieve the desired efficiencies. For instance, $BaZrS_3$ samples prepared with the a-facets could be utilized in improving the optical absorption properties and the thermoelectric efficiencies as this lattice direction exhibits marginally lower lattice thermal conductivity, relatively lower electronic thermal conductivity, higher Seebeck coefficient but only slightly lower in electrical conductivity as compared to the b- facets of the crystals.

κ_e reveals directional dependence at $T > 150$ K and exhibits low magnitudes relative to $CaZrSe_3$ and other similar compounds.[20] The directional dependence is akin to that observed for σ. An ultra-low mean $\kappa_e \approx 0.004$ $Wm^{-1}K^{-1}$ is predicted at 300 K and is attributed to the low carrier mobility compared to those through SnSe, GeS, GeSe and SnS lattices. From Figure 4(c) we note that κ_e increases rather linearly with temperature as more carriers are excited at higher T. A similar trend is observed under n-type doping (Figure S4(c)), while the highest κ_e are obtained along the a and b lattice directions for both p-type and n-type doping, analogous to σ.

The variation of PF with T presented in Figure 4(d), shows that PF increases from 50 K to 350 K and decreases at $T > 350$ K. Nevertheless, PF increases from 50 to 1000 K for n-type doped $BaZrS_3$, while the highest $PF = 0.135$ $\mu Wcm^{-1}K^{-2}$ is achieved at 350 K for p-type doping with room temperature $PF \approx 0.133$ $\mu Wcm^{-1}K^{-2}$. These predictions are lower than that of other chalcogenide perovskites[21] due to the relatively low σ of $BaZrS_3$.

The variations of S, σ, κ_e and PF with chemical potential μ at different temperatures are reproduced in Figure 5. μ essentially mimics the intensity with which $BaZrS_3$ is doped, and also determines the center of the Fermi-Dirac distribution function that governs the probability of occupation of a quantum state with energy E. We predict a high $S \approx 3000$ μV/K at 300 K for $\mu \approx 0.1$ eV, which is higher than that for $CaZrSe_3$ (2300 μV/K)[21] and significantly greater than that of other competing electronic materials[20] (highest $S \approx 2000$ μV/K for GeS).

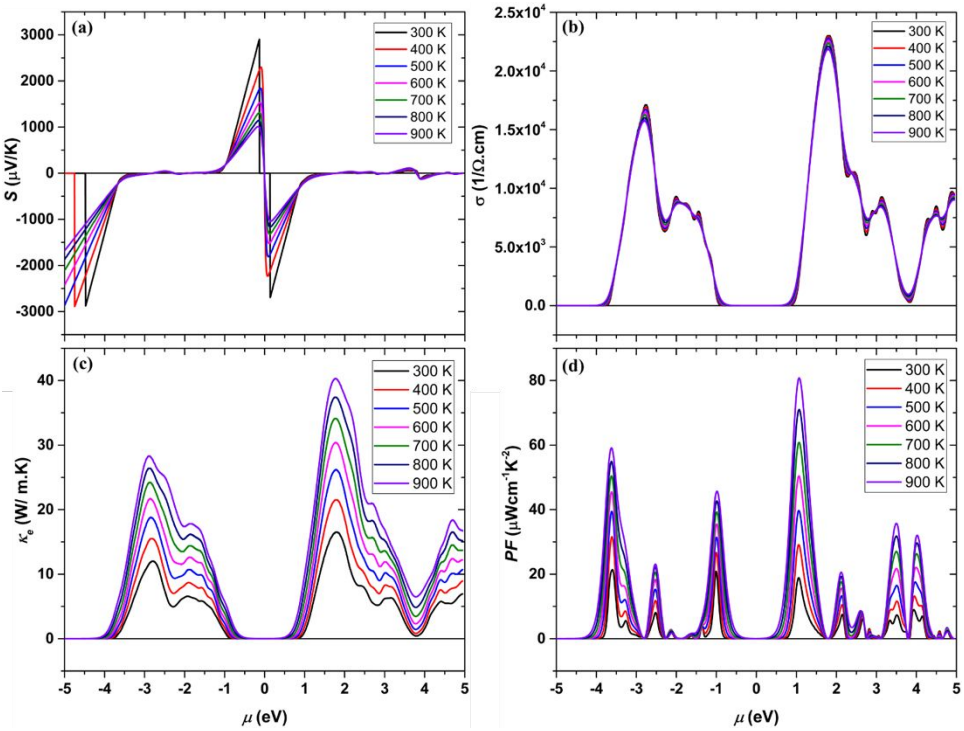

Figure 5: Electronic transport properties as a function of chemical potential μ for $BaZrS_3$. **(a)** Seebeck coefficient S, **(b)** electrical conductivity σ, **(c)** electronic thermal conductivity κ_e, **(d)** power factor PF, all across a range of temperatures. S is highest within a short chemical potential range in the neighborhood of 0 eV. Both σ and κ_e attain higher values for $\mu > 1$ eV and < -1 eV. The highest PF is achieved for $\mu \approx 1.2$ eV.

As T increases from 300 K to 600 K, S reduces to ~ 1500 μV/K due to the increased entropy. Also, S being inversely proportional to T, as noted in the correlation between S and Peltier coefficient[25], contributes to this variation. The peak S values are obtained for μ in the range of 0±0.2 eV. On the other hand, while σ varies nonlinearly with μ, the highest σ are achieved at $\mu \approx -2.8$ eV and 1.8 eV. Note that $\sigma \approx 0$ eV at $\mu \approx \pm 0.5$ eV. Figure 5(b) also reveals how σ can be tuned with p-type (negative μ) and n-type (positive μ) doping. κ_e increases with T as observed from Figure 5(c) due to an increased number of carriers. The highest κ_e are achieved at $\mu \approx -3$ eV and 1.8 eV. Finally, the highest PF values are, thus, predicted for p-type doping at $\mu \approx -1$ eV, -3.6 eV and for n-type doping at $\mu \approx 1.2$ eV.

The evolution of the thermoelectricity relevant electronic transport properties, *viz.*, *S*, σ, and κ_e as a function of μ at 300 K is illustrated in Figure 6 to understand the underlying anisotropy in the different lattice directions for both *p*- and *n*-type doping. *S* exhibits no anisotropic effects, while σ and κ_e reveal strong directional dependence for -1< μ >1. The highest σ and κ_e are achieved along the *a* and *b* lattice directions for both *p*- and *n*-type doping. We corroborate that these variations are due to the low carrier effective mass along the corresponding lattice directions under doping.

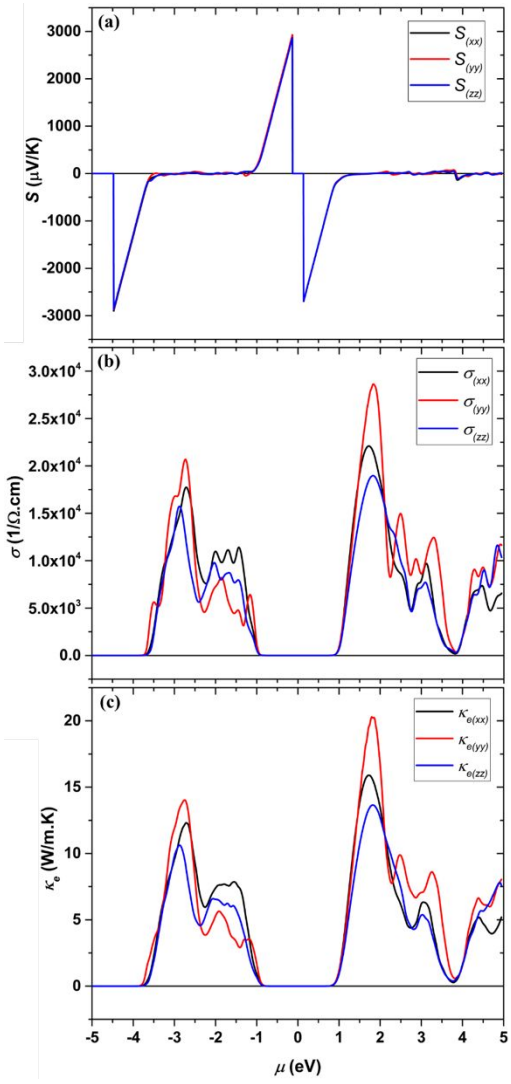

Figure 6: Anisotropic contributions to carrier transport at 300 K along the *a*, *b* and *c* lattice directions of $BaZrS_3$ to **(a)** the Seebeck coefficient *S*, **(b)** electrical conductivity σ, and **(c)** electronic thermal conductivity κ_e. *S* exhibits no anisotropic effects while σ and κ_e show strong dependencies, especially their high values along the *a* and *b* crystallographic directions.

The distribution of ZT_e with μ across different temperatures for both *p*- and *n*-type doping is presented in Figure 7. While no significant differences in ZT_e are noted, with respect to T at $\mu \approx \pm 1$ eV, we observe a high $ZT_e \approx 1$ at $\mu \approx \pm 1$ eV. The highest $ZT_e = 1.08$ is achieved at $\mu \approx -4.0$ eV as well as at higher μ values for *p*-type doping. The high ZT_e arises primarily due to a combination of high S and low κ_e of $BaZrS_3$. This result identifies a potential range for μ at which $BaZrS_3$ can be designed to achieve an optimum thermoelectric efficiency.

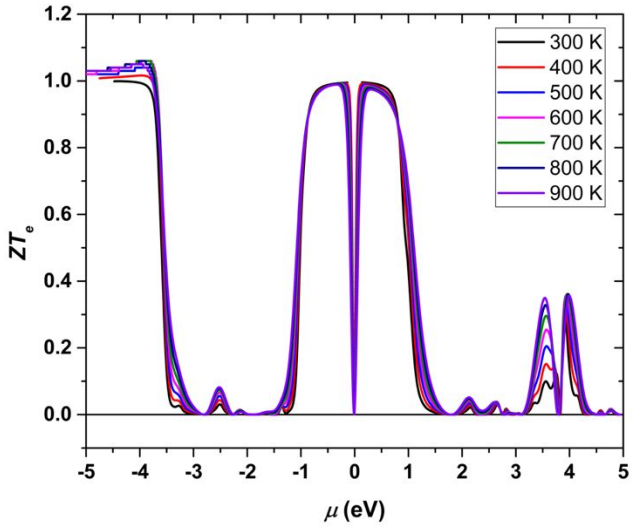

Figure 7: Upper limit of the thermoelectric figure of merit, ZT_e, for $BaZrS_3$ at different temperatures. A high ZT_e of ~1.08 is achieved at 300 K, while relatively higher ZT_e values are observed for *p*-type doping than for *n*-type doping.

CONCLUSION

We examine the electronic transport and optical properties of the distorted orthorhombic perovskite $BaZrS_3$. The material has an optical band gap of 1.79 eV that is in the neighborhood of the optimum band gap of 1.35 eV for single junction photovoltaic applications. At photon energies of 3 eV, we calculate a high optical absorption coefficient of 3×10^5 cm^{-1}. Also, there is an early onset to optical absorption at 0.5 eV that is significantly below the optical band gap. The power factor PF and upper limit of the thermoelectric figure of merit ZT_e are predicted at several carrier concentrations, while a carrier concentration of 10^{17} cm^{-3} is identified to yield optimum properties,

where we calculate the Seebeck coefficient S, electrical conductivity σ, and electron thermal conductivity κ_e.

The highest S is observed for p-type doping relative to n-type doping while σ produces high values for n-type doping compared to p-type doping. The electronic transport properties display strong directional dependence across all temperatures for both p- and n-type doping. The variation of the electronic properties with chemical potential μ for both p- and n-type doping reveals that $BaZrS_3$ exhibits high $S \approx 3000$ μV/K when doped within a narrow chemical potential range of 0±0.3 eV. The highest σ are observed when $BaZrS_3$ is doped at $\mu \approx$ -2.8 eV and 1.8 eV while the highest PF values are achieved at chemical potentials $\mu \approx$ -1 eV and -3.5 eV for p-type doping and $\mu \approx 1.2$ eV for n-type doping. Thus, the highest PF is observed for n-type doping due to the corresponding higher electrical conductivity (~ 2× that of p-type doping). Strong anisotropic dependencies are observed along the a and b lattice directions for σ and κ_e for p-type and n-type doping. The highest $ZT_e \approx 1.0$ and 1.08 achieved at $\mu \approx \pm 1$ and -4 eV, respectively, together with lattice conductivities,[15] suggests that $BaZrS_3$ holds potential for thermoelectric applications, as has been also suggested previously,[42] in addition to its capability for high photovoltaic performance.

METHODS

Mermin's finite temperature DFT[26] implemented in the Vienna ab initio Simulation Package (VASP)[27] is used to perform all the DFT calculations. Ba, Zr and S atoms electronic configurations are represented by $[Xe]6s^2$, $[Kr]4d^25s^2$ and $[Ne]3s^23p^4$ respectively. The core part of the valence electron wavefunctions, which are constrained, as well as the valence electron wavefunctions are represented by the Projector Augmented Wavefunction (PAW) pseudopotentials.[28] The number of planewaves that are needed to effectively describe the electrons close to the nuclei are significantly reduced with the use of the PAW pseudopotentials. The unit cell and atomic positions are relaxed using the PBEsol[29] functional for solids while the Methfessel-Paxton[30] smearing scheme is utilized with the gamma parameter set to 0.1 eV. An energy cut-off of 600 eV is used for the planewave expansion. A Monkhorst-Pack[31] special grid sampling of the k-points for integration of the Brillouin zone yields 7 × 5 × 7 k-points representing 123 irreducible number of sampling points for all bulk calculations. Resolution of the Kohn-Sham equations is achieved by using the self-consistent field procedure and setting energy changes for each cycle at 10^{-4} eV as the convergence

criterion between two successive iterations. The distorted orthorhombic structure of $BaZrS_3$ is illustrated in Figure 8. For the band gap and the optical absorption spectrum calculations, the hybrid HSE06 functional[32] is used. The mixing parameter α that controls the amount of the Hartree-Fock exchange energy is set to 0.25, while the long-range part of the exchange (ω) is set to 0.2 $Å^{-1}$.

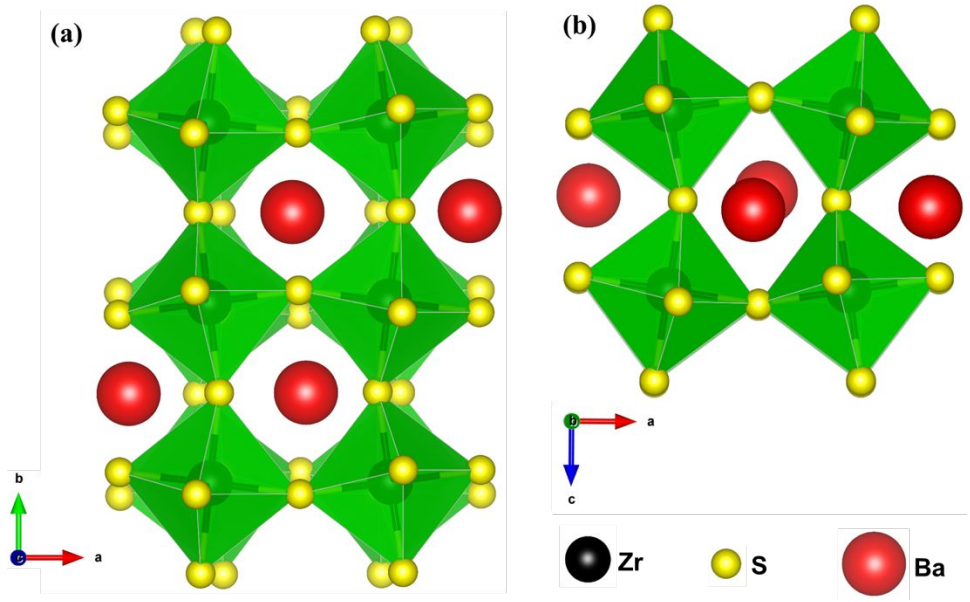

Figure 8: (a) Side and (b) top views of the distorted perovskite structure of $BaZrS_3$.

The transport properties are determined using the linearized Boltzmann transport equation in the relaxation time approximation as implemented in the BoltzTraP[18] code. The code uses a Fourier expansion of the electronic energies calculated from VASP for the optimized structures. A denser k-mesh of 120,000 points is used to ensure accurate transport properties are predicted. The thermoelectric figure of merit $ZT = \frac{S^2\sigma T}{\kappa_e + \kappa_L} = \frac{S^2\sigma}{\kappa_e} \cdot \frac{\kappa_e}{\kappa_e + \kappa_L} T$, where S is the Seebeck coefficient, σ is the electrical conductivity, T is temperature, κ_e *and* κ_L are the electronic thermal and lattice thermal conductivities, respectively. $\frac{S^2\sigma}{\kappa_e} T$ = ZT_e denotes the upper limit of ZT. Although S is independent of the relaxation time τ, σ and κ_e are dependent on the choice of τ. Here, we use τ = 10^{-14} s, which yields predictions that concur with experimental measurements.[19,20] The Sumo Python toolkit is used to characterize the electronic band structure and the UV-VIS absorption

spectrum.[33] The carrier relaxation time is calculated using the electron-phonon (optical and acoustic) interaction as implemented in the Electron-Phonon Wannier (EPW) code.[34,35]

All self-consistent (SCF), non self-consistent (non-SCF) and phonon calculations needed for the electron-phonon coupling matrix are performed with the Quantum-Espresso (QE)[36–38] package. Initially, we calculate the Kohn-Sham wavefunctions and Eigenvalues through the Brillouin zone of the crystal using an SCF, followed by a non-SCF which provides the DFT band structure with an under-estimated band gap as compared to the HSE06 band gap. This process was followed by a full phonon spectrum calculation using a 3 × 3 × 3 coarse q-grid, yielding 8 irreducible q-points. We scrutinize the phonon spectrum and find no imaginary frequency pockets as we have reported previously.[15] This data is used in constructing the dynamical matrix required for computing the electron-phonon coupling matrix. In the first part of the EPW calculation, the coarse 3 × 3 × 3 phonon q-grid is interpolated onto a fine 120 × 120 × 120 grid in combination with the k-point path employed to determine the electronic band structure. For obtaining the electron-phonon coupling constant, we use the Maximally Localized Wannier Functions (MLWF)[39–41] to interpolate the electronic band structure. The interpolation is performed by projecting the Wannier functions on the Zr- d and S- p orbitals since these contribute the most to the conduction and valence bands around the Fermi level as can be noted from Figure 1. Additionally, in the Wannier interpolation scheme, we select a disentanglement window between 5.5 eV to -2.5 eV while the frozen window is selected to be between 5.0 eV to -1.5 eV. The electron self-energy Σ_{nk} for band n and state k is derived from the interpolated dense electron-phonon coupling matrix elements, while the relaxation time τ is calculated from the scattering rate using $(\tau_{nk})^{-1} = 2[\mathrm{Im}(\sum_{nk})]/\hbar$, where $\hbar$ is the reduced Planck constant. The imaginary part of the electron self-energy is used in estimating the scattering rate at different temperatures. Thus, the relaxation time was calculated using the self-energy relaxation time approximation as implemented in the EPW code as *scattering_serta*.

ACKNOWLEDGMENT

The work by E. O.-A. and G.B. was supported, in part, by the National Science Foundation (NSF) through award CMMI-1753770. The computations were carried out on the cluster Sol managed by the Library and Technology Services Research Computing at Lehigh University. N.K. acknowledges funding support from the NSF (award # 2013640).

AUTHOR CONTRIBUTIONS

E. O.-A. designed the project, performed the calculations and analyzed the results. All authors contributed in the discussion of the results and the writing of the manuscript.

DATA AVAILABILITY

The data generated from the simulations are available from the corresponding author upon reasonable request.

COMPETING INTERESTS

The authors declare no competing interests.

REFERENCES

(1) Lee, C.-S.; Kleinke, K. M.; Kleinke, H. Synthesis, Structure, and Electronic and Physical Properties of the Two SrZrS3 Modifications. *Solid State Sciences* **2005**, *7* (9), 1049–1054. https://doi.org/10.1016/j.solidstatesciences.2005.02.010.

(2) Clearfield, A. The Synthesis and Crystal Structures of Some Alkaline Earth Titanium and Zirconium Sulfides. *Acta Crystallographica* **1963**, *16* (2), 135–142. https://doi.org/10.1107/S0365110X6300030X.

(3) Nitta, T.; Nagase, K.; Hayakawa, S. Formation, Microstructure, and Properties of Barium Zirconium Sulfide Ceramics. *Journal of the American Ceramic Society* **1970**, *53* (11), 601–604. https://doi.org/10.1111/j.1151-2916.1970.tb15981.x.

(4) Lelieveld, R.; IJdo, D. J. W. Sulphides with the $GdFeO_3$ Structure. *Acta Crystallographica Section B Structural Crystallography and Crystal Chemistry* **1980**, *36* (10), 2223–2226. https://doi.org/10.1107/S056774088000845X.

(5) Wang, Y.; Sato, N.; Fujino, T. Synthesis of BaZrS3 by Short Time Reaction at Lower Temperatures. *Journal of Alloys and Compounds* **2001**, *327* (1), 104–112. https://doi.org/10.1016/S0925-8388(01)01553-5.

(6) Wang, Y.; Sato, N.; Yamada, K.; Fujino, T. Synthesis of BaZrS3 in the Presence of Excess Sulfur. *Journal of Alloys and Compounds* **2000**, *311* (2), 214–223. https://doi.org/10.1016/S0925-8388(00)01134-8.

(7) Tranchitella, L. J.; Chen, B.-H.; Fettinger, J. C.; Eichhorn, B. W. Structural Evolutions in the Sr1−xBaxZrSe3Series. *Journal of Solid State Chemistry* **1997**, *130* (1), 20–27. https://doi.org/10.1006/jssc.1996.7253.

(8) Takeda, Y.; Kanamura, F.; Shimada, M.; Koizumi, M. The Crystal Structure of BaNiO3. *Acta Crystallographica Section B* **1976**, *32* (8), 2464–2466. https://doi.org/10.1107/S056774087600798X.

(9) Sun, Y.-Y.; Agiorgousis, M. L.; Zhang, P.; Zhang, S. Chalcogenide Perovskites for Photovoltaics. *Nano Lett.* **2015**, *15* (1), 581–585. https://doi.org/10.1021/nl504046x.

(10) Polfus, J. M.; Norby, T.; Bredesen, R. Protons in Oxysulfides, Oxysulfates, and Sulfides: A First-Principles Study of La2O2S, La2O2SO4, SrZrS3, and BaZrS3. *J. Phys. Chem. C* **2015**, *119* (42), 23875–23882. https://doi.org/10.1021/acs.jpcc.5b08278.

(11) Shockley, W.; Queisser, H. J. Detailed Balance Limit of Efficiency of P-n Junction Solar Cells. *Journal of Applied Physics* **1961**, *32* (3), 510–519. https://doi.org/10.1063/1.1736034.

(12) Meng, W.; Saparov, B.; Hong, F.; Wang, J.; Mitzi, D. B.; Yan, Y. Alloying and Defect Control within Chalcogenide Perovskites for Optimized Photovoltaic Application. *Chem. Mater.* **2016**, *28* (3), 821–829. https://doi.org/10.1021/acs.chemmater.5b04213.

(13) Gross, N.; Sun, Y.-Y.; Perera, S.; Hui, H.; Wei, X.; Zhang, S.; Zeng, H.; Weinstein, B. A. Stability and Band-Gap Tuning of the Chalcogenide Perovskite ${\mathrm{BaZrS}}_{3}$ in Raman and Optical Investigations at High Pressures. *Phys. Rev. Applied* **2017**, *8* (4), 044014. https://doi.org/10.1103/PhysRevApplied.8.044014.

(14) Bennett, J. W.; Grinberg, I.; Rappe, A. M. Effect of Substituting of S for O: The Sulfide Perovskite ${\text{BaZrS}}_{3}$ Investigated with Density Functional Theory. *Phys. Rev. B* **2009**, *79* (23), 235115. https://doi.org/10.1103/PhysRevB.79.235115.

(15) Osei-Agyemang, E.; Balasubramanian, G. Understanding the Extremely Poor Lattice Thermal Transport in Chalcogenide Perovskite BaZrS3. *ACS Appl. Energy Mater.* **2020**, *3* (1), 1139–1144. https://doi.org/10.1021/acsaem.9b02185.
(16) Perera, S.; Hui, H.; Zhao, C.; Xue, H.; Sun, F.; Deng, C.; Gross, N.; Milleville, C.; Xu, X.; Watson, D. F.; Weinstein, B.; Sun, Y.-Y.; Zhang, S.; Zeng, H. Chalcogenide Perovskites – an Emerging Class of Ionic Semiconductors. *Nano Energy* **2016**, *22*, 129–135. https://doi.org/10.1016/j.nanoen.2016.02.020.
(17) Chandola, A.; Kim, H. J.; Dutta, P. S.; Guha, S.; Gonzalez, L.; Kumar, V. Below Band-Gap Optical Absorption in GaxIn1−xSb Alloys. *Journal of Applied Physics* **2005**, *98* (9), 093103. https://doi.org/10.1063/1.2128042.
(18) Madsen, G. K. H.; Singh, D. J. BoltzTraP. A Code for Calculating Band-Structure Dependent Quantities. *Computer Physics Communications* **2006**, *175* (1), 67–71. https://doi.org/10.1016/j.cpc.2006.03.007.
(19) Yabuuchi, S.; Okamoto, M.; Nishide, A.; Kurosaki, Y.; Hayakawa, J. Large Seebeck Coefficients of Fe2TiSn and Fe2TiSi: First-Principles Study. *Appl. Phys. Express* **2013**, *6* (2), 025504. https://doi.org/10.7567/APEX.6.025504.
(20) Ding, G.; Gao, G.; Yao, K. High-Efficient Thermoelectric Materials: The Case of Orthorhombic IV-VI Compounds. *Scientific Reports* **2015**, *5*, 9567. https://doi.org/10.1038/srep09567.
(21) Osei-Agyemang, E.; Adu, C. E.; Balasubramanian, G. Doping and Anisotropy–Dependent Electronic Transport in Chalcogenide Perovskite CaZrSe3 for High Thermoelectric Efficiency. *Advanced Theory and Simulations 0* (0), 1900060. https://doi.org/10.1002/adts.201900060.
(22) Irkhin Yu. V; Irkhin Yu. P. *Electronic Structure, Correlated Effects and Physical Properties of d- and f-Metals and Their Compounds*; Cambridge International Science Publishing, 2007.
(23) Mehdizadeh Dehkordi, A.; Zebarjadi, M.; He, J.; Tritt, T. M. Thermoelectric Power Factor: Enhancement Mechanisms and Strategies for Higher Performance Thermoelectric Materials. *Materials Science and Engineering: R: Reports* **2015**, *97*, 1–22. https://doi.org/10.1016/j.mser.2015.08.001.
(24) He, J.; Tritt, T. M. Advances in Thermoelectric Materials Research: Looking Back and Moving Forward. *Science* **2017**, *357* (6358), eaak9997. https://doi.org/10.1126/science.aak9997.
(25) Gunnarshaug, A. F.; Kjelstrup, S.; Bedeaux, D. The Heat of Transfer and the Peltier Coefficient of Electrolytes. *Chemical Physics Letters: X* **2020**, *5*, 100040. https://doi.org/10.1016/j.cpletx.2019.100040.
(26) Mermin, N. D. Thermal Properties of the Inhomogeneous Electron Gas. *Physical Review* **1965**, *137* (5A), A1441–A1443.
(27) Hafner, J. Ab-Initio Simulations of Materials Using VASP: Density-Functional Theory and Beyond. *Journal of Computational Chemistry* **2008**, *29* (13), 2044–2078.
(28) Kresse, G.; Joubert, D. From Ultrasoft Pseudopotentials to the Projector Augmented-Wave Method. *Physical Review B - Condensed Matter and Materials Physics* **1999**, *59* (3), 1758–1775.
(29) Perdew, J. P.; Ruzsinszky, A.; Csonka, G. I.; Vydrov, O. A.; Scuseria, G. E.; Constantin, L. A.; Zhou, X.; Burke, K. Restoring the Density-Gradient Expansion for Exchange in Solids

and Surfaces. *Phys. Rev. Lett.* **2008**, *100* (13), 136406. https://doi.org/10.1103/PhysRevLett.100.136406.

(30) Methfessel, M.; Paxton, A. T. High-Precision Sampling for Brillouin-Zone Integration in Metals. *Physical Review B* **1989**, *40* (6), 3616–3621.

(31) Monkhorst, H. J.; Pack, J. D. Special Points for Brillouin-Zone Integrations. *Physical Review B* **1976**, *13* (12), 5188–5192.

(32) Heyd, J.; Scuseria, G. E.; Ernzerhof, M. Hybrid Functionals Based on a Screened Coulomb Potential. *J. Chem. Phys.* **2003**, *118* (18), 8207–8215. https://doi.org/10.1063/1.1564060.

(33) Ganose, A. M.; Jackson, A. J.; Scanlon, D. O. Sumo: Command-Line Tools for Plotting and Analysis of Periodic *ab Initio* Calculations. *Journal of Open Source Software* **2018**, *3* (28), 717. https://doi.org/10.21105/joss.00717.

(34) Noffsinger, J.; Giustino, F.; Malone, B. D.; Park, C.-H.; Louie, S. G.; Cohen, M. L. EPW: A Program for Calculating the Electron–Phonon Coupling Using Maximally Localized Wannier Functions. *Computer Physics Communications* **2010**, *181* (12), 2140–2148. https://doi.org/10.1016/j.cpc.2010.08.027.

(35) Poncé, S.; Margine, E. R.; Verdi, C.; Giustino, F. EPW: Electron–Phonon Coupling, Transport and Superconducting Properties Using Maximally Localized Wannier Functions. *Computer Physics Communications* **2016**, *209*, 116–133. https://doi.org/10.1016/j.cpc.2016.07.028.

(36) Giannozzi, P.; Andreussi, O.; Brumme, T.; Bunau, O.; Nardelli, M. B.; Calandra, M.; Car, R.; Cavazzoni, C.; Ceresoli, D.; Cococcioni, M.; Colonna, N.; Carnimeo, I.; Corso, A. D.; Gironcoli, S. de; Delugas, P.; DiStasio, R. A.; Ferretti, A.; Floris, A.; Fratesi, G.; Fugallo, G.; Gebauer, R.; Gerstmann, U.; Giustino, F.; Gorni, T.; Jia, J.; Kawamura, M.; Ko, H.-Y.; Kokalj, A.; Küçükbenli, E.; Lazzeri, M.; Marsili, M.; Marzari, N.; Mauri, F.; Nguyen, N. L.; Nguyen, H.-V.; Otero-de-la-Roza, A.; Paulatto, L.; Poncé, S.; Rocca, D.; Sabatini, R.; Santra, B.; Schlipf, M.; Seitsonen, A. P.; Smogunov, A.; Timrov, I.; Thonhauser, T.; Umari, P.; Vast, N.; Wu, X.; Baroni, S. Advanced Capabilities for Materials Modelling with Quantum ESPRESSO. *J. Phys.: Condens. Matter* **2017**, *29* (46), 465901. https://doi.org/10.1088/1361-648X/aa8f79.

(37) Giannozzi, P.; Baroni, S.; Bonini, N.; Calandra, M.; Car, R.; Cavazzoni, C.; Ceresoli, D.; Chiarotti, G. L.; Cococcioni, M.; Dabo, I.; Corso, A. D.; Gironcoli, S. de; Fabris, S.; Fratesi, G.; Gebauer, R.; Gerstmann, U.; Gougoussis, C.; Kokalj, A.; Lazzeri, M.; Martin-Samos, L.; Marzari, N.; Mauri, F.; Mazzarello, R.; Paolini, S.; Pasquarello, A.; Paulatto, L.; Sbraccia, C.; Scandolo, S.; Sclauzero, G.; Seitsonen, A. P.; Smogunov, A.; Umari, P.; Wentzcovitch, R. M. QUANTUM ESPRESSO: A Modular and Open-Source Software Project for Quantum Simulations of Materials. *J. Phys.: Condens. Matter* **2009**, *21* (39), 395502. https://doi.org/10.1088/0953-8984/21/39/395502.

(38) Giannozzi, P.; Baseggio, O.; Bonfà, P.; Brunato, D.; Car, R.; Carnimeo, I.; Cavazzoni, C.; de Gironcoli, S.; Delugas, P.; Ferrari Ruffino, F.; Ferretti, A.; Marzari, N.; Timrov, I.; Urru, A.; Baroni, S. Quantum ESPRESSO toward the Exascale. *J. Chem. Phys.* **2020**, *152* (15), 154105. https://doi.org/10.1063/5.0005082.

(39) Mostofi, A. A.; Yates, J. R.; Pizzi, G.; Lee, Y.-S.; Souza, I.; Vanderbilt, D.; Marzari, N. An Updated Version of Wannier90: A Tool for Obtaining Maximally-Localised Wannier Functions. *Computer Physics Communications* **2014**, *185* (8), 2309–2310. https://doi.org/10.1016/j.cpc.2014.05.003.

(40) Marzari, N.; Vanderbilt, D. Maximally Localized Generalized Wannier Functions for Composite Energy Bands. *Phys. Rev. B* **1997**, *56* (20), 12847–12865. https://doi.org/10.1103/PhysRevB.56.12847.
(41) Souza, I.; Marzari, N.; Vanderbilt, D. Maximally Localized Wannier Functions for Entangled Energy Bands. *Phys. Rev. B* **2001**, *65* (3), 035109. https://doi.org/10.1103/PhysRevB.65.035109.
(42) Gupta, T.; Ghoshal, D.; Yoshimura, A.; Basu, S.; Chow, P. K.; Lakhnot, A. S.; Pandey, J.; Warrender, J. M.; Efstathiadis, H.; Soni, A.; Osei-Agyemang, E.; Balasubramanian, G.; Zhang, S.; Shi, S.-F.; Lu, T.-M.; Meunier, V.; Koratkar, N. An Environmentally Stable and Lead-Free Chalcogenide Perovskite *Advanced Functional Materials* **2020**, 30 (23), 2001387. https://doi.org/10.1002/adfm.202001387.